Electronic Supplementary Information

Composition-dependent emission linewidth broadening in lead bromide perovskite ($APbBr_3$, A = Cs and CH_3NH_3) nanoparticles

Sujin Ham,[a] Heejae Chung,[a] Tae-Woo Kim,[a] Jiwon Kim,[b] and Dongho Kim[a]*

[a] Spectroscopy Laboratory for Functional π-Electronic Systems and Department of Chemistry, Yonsei University, 50 Yonsei-ro, Seodaemun-gu, Seoul, 03722, Republic of Korea

[b] School of Integrated Technology and Underwood International College, Yonsei University, 85 Songdogwahak-ro, Yeonsu-gu, Incheon 21983, Republic of Korea.

Corresponding Author: dongho@yonsei.ac.kr (D. Kim)

Table of Contents

1. Experimental

Sample preparation

$CsPbBr_3$ and **$MAPbBr_3$** nanoparticles (NPs) were synthesized by following the procedures reported in previous studies.[S1,S2] A typical synthesis of $CsPbBr_3$ (or $MAPbBr_3$) NPs involved sequentially co-dissolving 0.4 mmol $PbBr_2$, 0.1 mL oleylamine, 1 mL oleic acid, and 0.4 mmol CsBr (or MABr) with ultrasonic agitation after each step in 10 mL DMF to form a clear transparent solution. Subsequently, 0.5 mL of precursor solution was quickly injected into each solution accompanied by vigorous stirring. A strong green emission was observed immediately after the injection. Centrifugation was performed at 3000 rpm for 20 min to sediment insoluble precipitates, and a bright supernatant solution was obtained. Samples for single-molecule confocal measurements were prepared by spin-coating NP solutions on rigorously cleaned coverslips at 3000 rpm for 30 s. The NP solutions were composed of NPs in toluene that contained 20 mg ml^{-1} polystyrene. Transmission electron microscopy images were acquired by JEOL JEM-ARM 200F at 200kV.

Ensemble spectroscopy

Steady-state absorption spectra were recorded by using a UV/Vis spectrometer (Cary5000, Varian). Steady-state fluorescence (excitation wavelength of 420 nm) of NPs in toluene was measured by using a fluorescence spectrophotometer (F-2500, Hitachi).

Defocused wide-field imaging measurements

Defocused wide-field imaging measurements were performed using an inverted optical microscope (IX71, Olympus) equipped with an oil immersion objective (1.4 NA, 100×, Plan Fluorite, Olympus) and a highly sensitive and cooled 512 × 512 pixel EMCCD camera (iXon Ultra, Andor). For excitation purpose, 420 nm light from a CW laser (LDH-D-C-420, Picoquent) was used with a power density corresponding to an average number of excitons per pulse, $\langle N_x \rangle = 0.1$. The circular polarized laser beam was sent to the microscope after passing through a laser line filter (FF01-420/10-25, Semrock), collimating lens, and dichroic mirror (T425lpxr, Chroma Technology) and then focused on the back-focal plane of the objective. The defocused image was

obtained by shifting the sample plane 0.9 μm toward the objective from the focus position. The image was magnified 3.4 times by using a relay lens. Then spectrally filtered by using a notch filter (HNPF-420.0AR-1.0, Kaiser optical systems) and band pass filters (FF-01-430/LP-25, Semrock). The image integration time corresponded to 50 ms. The defocused fluorescence images were analyzed by using a pattern matching routine programmed in MatLab to approximately determine the transition dipole moment orientation by calculating two-dimensional correlation coefficients (r) of the defocused images that were experimentally (*A*) and theoretically (*B*) obtained by using the following equation:

$$r = \frac{\sum_m \sum_n (A_{mn} - \overline{A})(B_{mn} - \overline{B})}{\sqrt{(\sum_m \sum_n (A_{mn} - \overline{A})^2)(\sum_m \sum_n (B_{mn} - \overline{B})^2)}}$$

where *A* and *B* denote the means of *A* and *B*, respectively.[S3]

Single-molecule confocal microscopy at room temperature (RT)

Confocal microscope (TE2000-U, Nikon) was equipped with a sample scanning stage at RT. Circular polarized light from a picosecond pulsed diode laser (LDH-D-C-420, Picoquent, 1 MHz repetition rate, prepared using a Berek compensator (5540, New Focus)) excited the samples. It was passed through a laser line filter (FF01-420/10-25, Semrock) and collimating lens. Then, it subsequently focused on the sample via an oil immersion objective (Plan Fluor, 1.3 NA, 100×, Nikon) with a power density corresponding to an average number of excitons per pulse, $\langle N_x \rangle$ = 0.1. Fluorescent signals were passed through a dichroic mirror (T425lpxr, Chroma Technology), spectrally filtered using a notch filter (HNPF-420.0AR-1.0, Kaiser optical systems) and a band pass filter (FF-01-430/LP-25, Semrock), and then split by using a non-polarizing 50:50 beam splitter. Half of the fluorescence was dispersed via a spectrograph (SpectraPro 2150i, Princeton Instruments) and projected onto an EMCCD camera (PL PROEM:512B EMCCD, Princeton Instruments). The other half was detected by an avalanche photodiode (APD) module (SPCM-AQR-16-FC, EG&G). The fluorescent signal detected by the APD was registered by a time-correlated single photon counting (TCSPC) PC (SPC 830, Becker & Hickl). The TCSPC was operated in first-in-first-out regime in which the arrival time after the beginning of acquisition and the time lag with respect to the excitation pulse were stored for each detected photon. The the full-width half maximum (FWHM) of the overall instrumental response function approximately corresponded to 500–600 ps. The data were processed by using a BIFL data analyzer software

(Scientific Software Technologies Center) to obtain fluorescence intensity trajectories and the time-resolved fluorescence decays.

Single-molecule confocal microscopy at low temperature (LT)

Detection of single molecule fluorescence was performed with a confocal microscope (Eclipse Ti-U, Nikon) by mounting the sample inside a liquid nitrogen flow cryostat (Microstat-HiResII, Oxford Instruments) in vacuum. The sample was excited by a circularly polarized light from a picosecond pulsed diode laser (LDH-D-P-405, Picoquant, 405 nm, 1 MHz repetition rate) that was prepared by a Berek compensator (5540, New Focus) with a power density corresponding to an average number of excitons per pulse, $\langle N_x \rangle = 0.1$. Scanning lens was mounted on a XY translation stage (M-605.1DD, Physik Instrumente) to image the different sample areas. Identical lens was used to recollimate the laser beam. Following deflection by a reflective mirror (21015, Chroma Technology), the laser beam was focused onto the focal plane of the dry objective (CFI S Plan Fluor ELWD 40×, Nikon). The fluorescence was collected by using the same objective, traced back along the same pathway as the excitation beam, and then passed through a dichroic mirror (ZT405 rdcm, Chroma Technology). A notch filter (CNPF-405.0-1.0, Kaiser Optical Systems Inc.) was used in combination with long pass filters (HQ425lp, Chroma Technology and FF-01-430/LP-25, Semrock) to remove the Rayleigh scattered light and then split by using a non-polarizing 50:50 beam splitter. Half of the fluorescence was dispersed via a spectrograph (SpectraPro 2150i, Princeton Instruments) and projected onto an EMCCD camera (iXon, Andor Technology) to record the fluorescence emission spectrum. The other half was detected by using an APD (SPCM-AQRH-16-TR, Excelitas Technologies). The FWHM of the overall instrumental response function approximately corresponded to 250–300 ps. The rest is the same as the confocal microscopy at RT.

2. Supporting Table and Figures

Table S1. Statistical analysis of the emission patterns (percent) of **$CsPbBr_3$** and **$MAPbBr_3$** NPs.

	Bilobal	Circular
$CsPbBr_3$ NP	85%	15%
$MAPbBr_3$ NP	21%	79%

Table S2. Comparison of the full-width at half maximum ($FWHM_{each}$) of single NP spectrum of each binning time with the $FWHM_{avg}$ of the time-averaged spectrum of single NP.

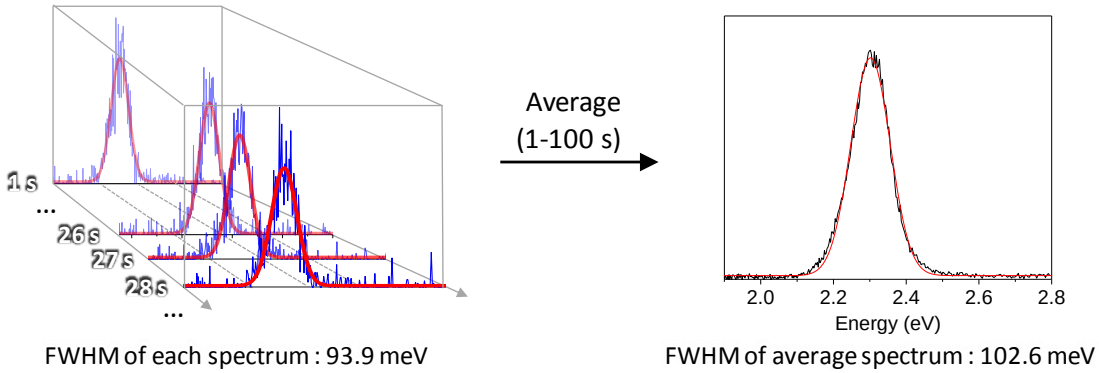

FWHM of each spectrum : 93.9 meV

FWHM of average spectrum : 102.6 meV

	$FWHM_{PL}$ (meV)	$FWHM_{each}$ (meV)	$FWHM_{avg}$ (meV)
$CsPbBr_3$ NP	117.2	93.2	95.5
$MAPbBr_3$ NP	134.8	93.9	102.6

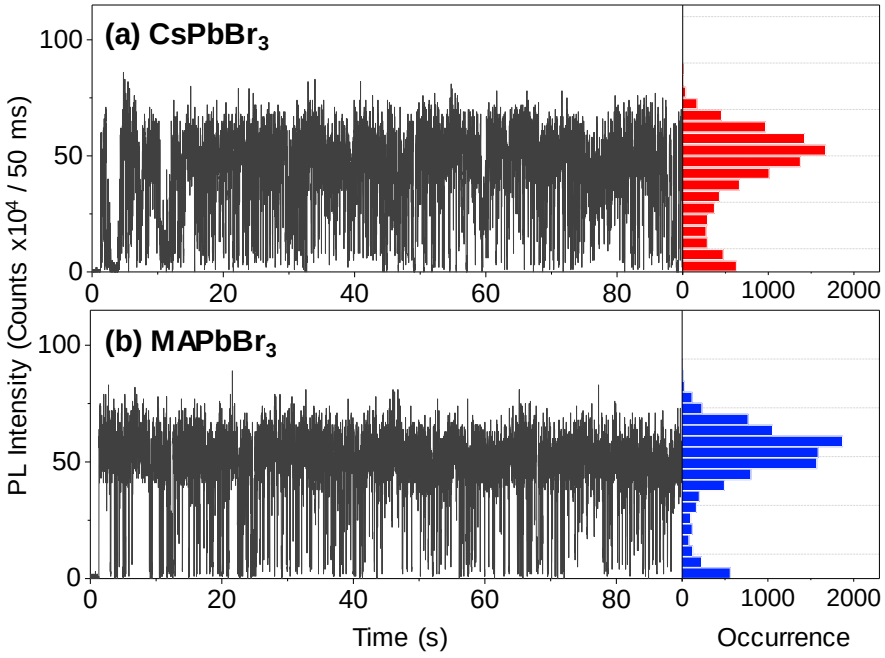

Fig. S1 Photoluminescence (PL) blinking dynamics for individual NPs: (a) **$CsPbBr_3$** NP and (b) **$MAPbBr_3$** NP. Each row presents the PL intensity trace (*left*) and the intensity histogram (*right*) of a single NP. The PL intensity histogram of **$CsPbBr_3$** NP is relatively broader than that of **$MAPbBr_3$** NP. This indicates that **$CsPbBr_3$** NPs have various states that magnify the counts in the tails of of the Gaussian distribution.

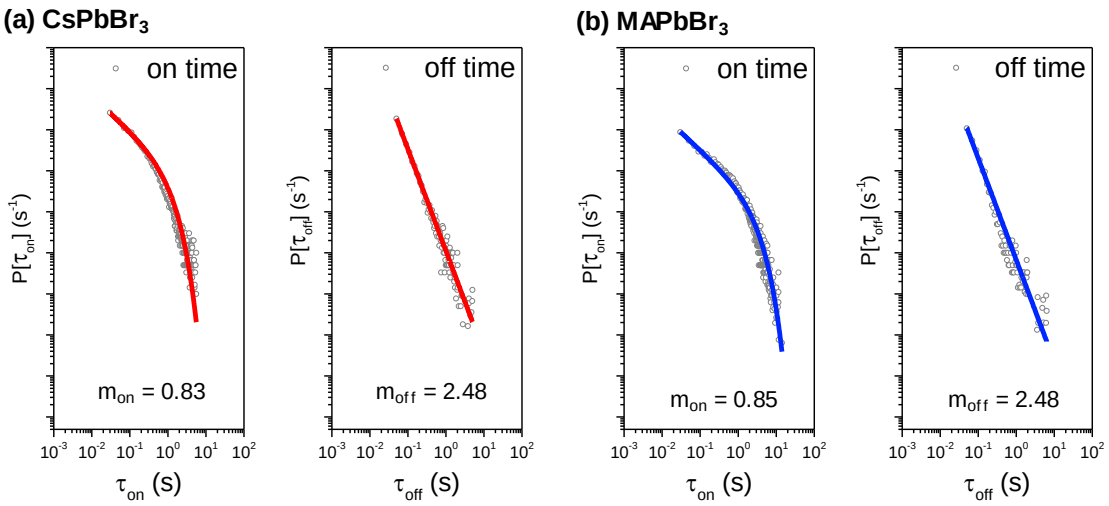

Fig. S2 Probability distributions for *on*- and *off*-times, calculated from more than 100 individual perovskite NPs to exclude any artifacts introduced by unexpected events. According to previously reported probability density plots, the probability densities for *off*-time events consistently follow a power-law distribution, whereas those for *on*-times showed "bending" structures for long *on*-time durations.[S4–S6] In our study, the *off*-time (blinking recovery) kinetics were observed not to be governed by a single rate constant for all samples because the probability densities were broadly distributed over a wide range of durations. Indeed, the blinking recovery kinetics were well fitted by a power law equation, $P(\tau_{off}) \propto \tau^{-m_{off}}$. In Contrast, the *on*-time kinetics followed a truncated power law behavior, $P(\tau_{on}) \propto \tau^{-m_{on}} e^{-\tau/\tau_{fall-off}}$, which shows a "bent" curvature for long values of τ_{on}. as previously reported by Wang et al.[S6,S7] In log–log plots, the power law coefficient is the slope of the linear fit, and the fall-off time ($\tau_{fall\text{-}off}$) indicates the start of exponential truncation.[S6–S8] This function can be used to describe a physical process which is governed by power law at short times and an exponential at long times due to the Auger recombination, which has been proposed for NP blinking.[S7–S12]

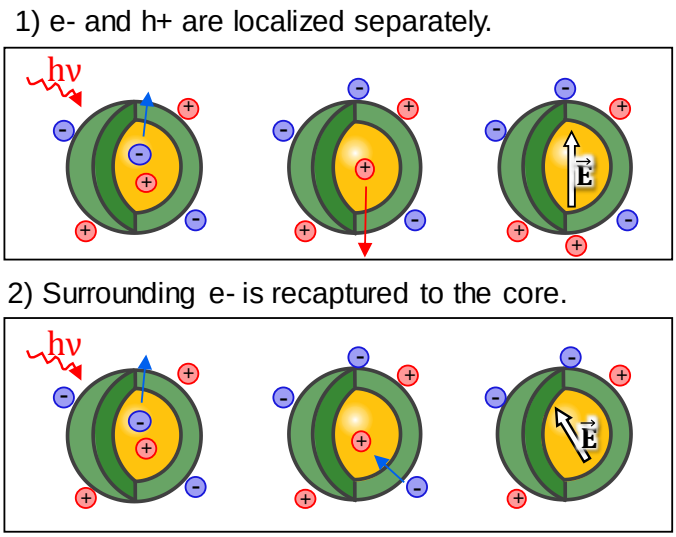

Fig. S3 Schematic representation of several possible mechanisms for changes in the local electric fields. After laser excitation and exciton formation, 1) an electron or hole from the exciton localizes near the surface of NP, leaving a delocalized charge carrier inside the core of NP. Following this initial charge localization due to ionization, the delocalized charge carrier can also be localized leading to a net of neutral core. 2) If the NP's environment is decorated by charges followed by process (1), then after subsequent ionization, a charge localized in the NP's environment can relax back into the nanoparticle core, recombining with the delocalized charge carrier.

3. References for Supporting Information

(S1) X. Li, Y. Wu, S. Zhang, B. Cai, Y. Gu, J. Song, H. Zeng, *Adv. Funct. Mater.*, 2016, **26**, 2435–2445.

(S2) H. Huang, A. S. Susha, S. V. Kershaw, T. F. Hung, A. L. Rogach, *Adv. Sci.*, 2015, **2**, 1500194.

(S3) S. Habuchi, T. Oba, M. Vacha, *Phys. Chem. Chem. Phys.,* 2011, **13**, 7001–7007.

(S4) A. A. Cordones, S. R. Leone, *Chem. Soc. Rev.*, 2013, **42**, 3209–3221.

(S5) J. J. Peterson, D. J. Nesbitt, *Nano Lett.*, 2009, **9**, 338–345.

(S6) S. F. Lee, M. A. Osborne, *ChemPhysChem*, 2009, **10**, 2174–2191.

(S7) S. Wang, C. Querner, T. Emmons, M. Drndic, C. H. Crouch, *J. Phys. Chem. B*, 2006, **110**, 23221–23227.

(S8) H. Chung, K. S. Cho, W. Koh, D. Kim, J. Kim, *Nanoscale*, 2016, **8**, 14109–14116.

(S9) I. H. Chung, M. G. Bawendi, *Phys. Rev. B*, 2004, **70**, 165304.

(S10) J. Tang, R. A. Marcus, *J. Chem. Phys*., 2005, **123**, 05474.

(S11) J. Tang, R. A. Marcus, *Phys. Rev. Lett*., 2005, **95**, 107401.

(S12) J. Tang, R. A. Marcus, *J. Chem. Phys*. 2005, **123**, 204511.